Near-Infrared Afterglow Luminescence Amplification *via* Albumin Complexation of Semiconducting Polymer Nanoparticles for Surgical Navigation in *Ex Vivo* Porcine Models

Nathaniel Bendele,[1,2,‡] Ken Kitamura, [1,2,‡] Isabella Vasquez,[1,2,3] Asma Harun,[1,3] Indrajit Srivastava[1,3,]*

1. Department of Mechanical Engineering, Texas Tech University, Lubbock, Texas 79409, United States

2. Department of Chemistry & Biochemistry, Texas Tech University, Lubbock, Texas 79409, United States

3. Texas Center for Comparative Cancer Research (TC3R), Amarillo, Texas 79106, United States

‡ *These authors contributed equally*

* *Authors to whom correspondence should be addressed:* indrajit.srivastava@ttu.edu

KEYWORDS. afterglow imaging, semiconducting polymer nanoparticles, protein complexation, image-guided cancer surgery, signal-to-background ratio

ABSTRACT. Afterglow imaging, leveraging persistent luminescence following light cessation, has emerged as a promising modality for surgical interventions. However, the scarcity of efficient near-infrared (NIR) responsive afterglow materials, along with their inherently low brightness and lack of cyclic modulation in afterglow emission, has impeded their widespread adoption. Addressing these challenges requires a strategic repurposing of afterglow materials that improve on such limitations. Here, we have developed an afterglow probe, composed of bovine serum albumin (BSA) coated with an afterglow material, a semiconducting polymer dye (PFODBT/SP1), called BSA@SP1 demonstrating a substantial amplification of the afterglow luminescence (~3-fold) compared to polymer-lipid coated PFODBT (DSPE-PEG@SP1). This enhancement is believed to be attributed to the electron-rich matrix provided by BSA that immobilizes SP1 and enhances the generation of $^1O_2$ radicals, which improves the afterglow luminescence brightness. Through molecule docking, physicochemical characterization, and optical assessments, we highlight BSA@SP1's superior afterglow properties, cyclic afterglow behavior, long-term colloidal stability, and biocompatibility. Furthermore, we demonstrate superior tissue permeation profiling of afterglow signals of BSA@SP1's compared to fluorescence signals using *ex vivo* tumor-mimicking phantoms and various porcine tissue types (skin, muscle, and fat). Expanding on this, to showcase BSA@SP1's potential in image-guided surgeries, we implanted tumor-mimicking phantoms within porcine lungs and conducted direct comparisons between fluorescence and afterglow-guided interventions to illustrate the latter's superiority. Overall, our study introduces a promising strategy for enhancing current afterglow materials through protein complexation, resulting in both ultrahigh signal-to-background ratios and cyclic afterglow signals.

INTRODUCTION. Currently, surgical procedures are the prevalent approach to treating various forms of solid tumors.[1] The traditional methods to detect tumor margins rely upon palpitations and visual inspection that allows surgeons to differentiate between healthy tissues and cancer tissue. However, using such information to guide surgical incisions has shown to be error-prone, particularly because many cancers aren't palpable. This increases the risk of cancer recurrence following surgery.[2-4] Thus, a lot of emphasis has been directed toward the development of preoperative and intraoperative imaging methods tailored toward specific characteristics of the tumor.[5,6] This approach is crucial for helping surgeons remove as much tumor tissue as possible. In the realm of intraoperative imaging, fluorescence imaging stands out due to its high resolution, sensitivity, absence of radiation, and rapid feedback. In recent years, near-infrared (NIR) fluorescent dyes have emerged as promising tools for delineating tumor margins in both experimental cancer models and human patients.[7-9] However, conventional probes in the NIR-I fluorescent window (having emission wavelengths between 700 and 900 nm) have limitations that include shallow tissue penetration (~1–3 mm) and significant tissue autofluorescence, which diminish their effectiveness for fluorescence imaging-guided surgery (FIGS).[10,11]

Recently, afterglow luminescence, which refers to sustained luminescence after the cessation of excited light, has shown immense promise in advancing bioimaging applications [12-16], particularly in the realm of image-guided surgery and intraoperative imaging.[17-19] Notably, afterglow imaging obviates the need for real-time excitation, effectively mitigating background signals stemming from tissue autofluorescence, a common limitation in NIR-I fluorescence imaging.[20,21] Despite the advantages of afterglow luminescence for *in vivo* imaging, its widespread utility remains hampered by the dearth of efficient NIR-responsive afterglow materials. The existing materials often exhibit suboptimal brightness and lack cyclic modulation

in afterglow emission, posing challenges to their broader adoption. Addressing these limitations necessitates a strategic reevaluation and repurposing of extant NIR-responsive afterglow materials to augment their efficacy in intraoperative surgical guidance.

Albumin, a major protein in the body, plays a pivotal role in transporting diverse substances in the blood.[22] Bovine serum albumin (BSA), closely resembles human serum albumin (HSA) with ~80% sequence similarity, making it a cost-effective and readily purified carrier molecule. Its structural features enable it to bind both positively and negatively charged molecules, as well as hydrophilic and hydrophobic compounds.[23-25] Notably, when fluorescent dyes, particularly cyanine dyes, are covalently conjugated or supramolecular encapsulation with BSA, they have demonstrated several advantages including (i) enhancing fluorescence brightness and photostability, (ii) improved colloidal stability by shielding against from endogenous enzymatic degradation, and (iii) improved biocompatibility.[26,27] Recent advancements have extended BSA's utility to include the coating of aggregation-induced emission dyes[28] which have been shown to improve their photodynamic therapy efficacy. This improvement arises from BSA providing an electron-rich environment that promotes the generation of the type-I reactive oxygen species. However, to date, there are no studies that explore the potential of a BSA coating to boost the afterglow luminescence of afterglow substrates.

Here, we have developed an afterglow probe, BSA@SP1, which consists of bovine serum albumin (BSA) coated with a semiconducting polymer dye, Poly[2,7-(9,9-dioctylfluorene)-*alt*-4,7-bis(thiophen-2-yl)benzo-2,1,3-thiadiazole] (PFODBT/SP1). Specifically, we show that BSA coating imparts BSA@SPNs with superior afterglow luminescence properties when compared to conventional polymer encapsulation matrix, 1,2-Distearoyl-sn-glycero-3-phosphoethanolamine-

Poly(ethylene glycol) (DSPE-PEG) by ~3-fold, and cyclic afterglow behavior. We hypothesize such an enhancement could be attributed to the electron-rich matrix provided by BSA, which immobilizes PFODBT and enhances its generation of $^1O_2$ radical generation, thus improving the afterglow luminescence brightness. Our preliminary molecular docking studies reveal that PFODBT preferentially inserts into the hydrophobic pocket of BSA, imparting BSA@SP1 nanoparticles with improved colloidal stability and biocompatibility. Moreover, we showcase enhanced tissue permeation profiling by leveraging the afterglow capabilities of BSA@SP1 through experiments conducted on *ex vivo* tumor cell-mimicking phantoms[29,30] and various porcine tissue types (including skin, muscle, and fat), revealing their superior signal-to-background ratio compared to fluorescence imaging. Expanding on this, to assess its effectiveness in image-guided cancer surgeries, we implanted tumor-mimicking phantoms at various locations within the porcine lungs: (i) 0.5mm below the right inferior lobe, (ii) 5mm below the left inferior lobe, and (iii) within the thoracic cavity. Subsequently, we conducted direct comparative studies between fluorescence- and afterglow-guided surgical interventions, highlighting the superior performance of afterglow-assisted procedures. In summary, our approach of protein immobilization to enhance afterglow luminescence in existing materials holds significant promise, as it improves signal-to-background ratios, benefits from a low afterglow background, and exhibits cyclic afterglow luminescence. These attributes showcase how BSA modification of afterglow materials enhances their imaging capabilities and serves as a highly promising candidate for image-guided cancer surgery in *in vivo* models.

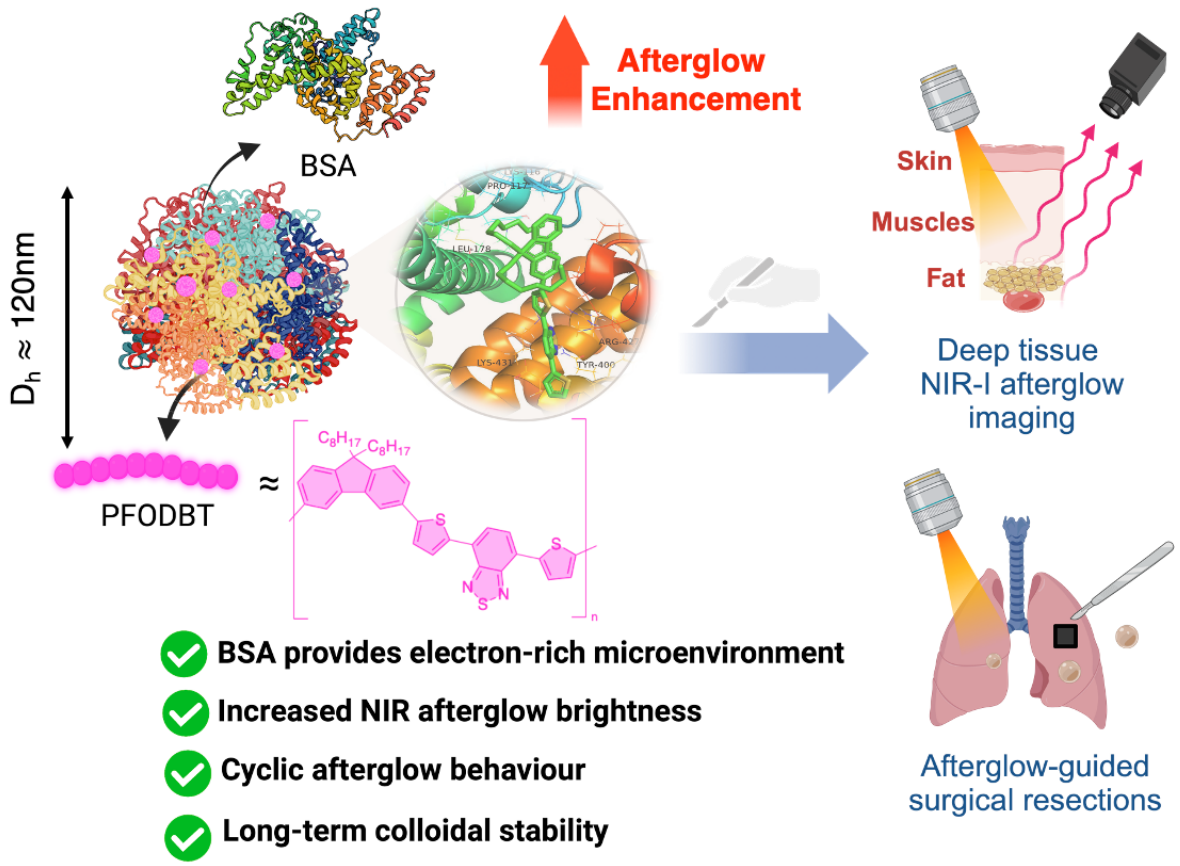

Figure 1. The schematic diagram illustrates the application of bovine serum albumin-coated PFODBT/SP1 semiconducting polymer nanoparticles (BSA@SP1). BSA@SP1 exhibits enhanced afterglow brightness and retention, long-term photostability, and colloidal stability. BSA@SP1 is further leveraged for deep tissue imaging and afterglow-guided surgical resection.

RESULTS AND DISCUSSION.

Synthesis of BSA@SPs. For the development of BSA@SP1 nanoparticles, a modified nanoprecipitation method was used (Figure 2a). SP1 (or PFODBT) was dissolved in THF and quickly added dropwise to BSA containing PBS1x solution under continuous probe sonication. For the development of our control nanoparticle, i.e. amphiphilic polymer (DSPE-PEG2k) coated SP1, i.e. DSPE-PEG@SP1, a general nanoprecipitation method was used. Both DSPE-PEG2k

and PFODBT were co-dissolved in THF and quickly added to PBS1x solution under continuous probe sonication. Once the post-processing that involved centrifugation wash steps was completed, it led to clear nanoparticle solutions (Figure 2b, c: insets) for use in further physicochemical and optical characterizations.

Physicochemical and Optical Characterization of BSA@SPs. The hydrodynamic diameter of DSPE-PEG@SP1 and BSA@SP1 were measured using dynamic light scattering (DLS) and showed sizes of ~108nm and ~125nm, respectively (Figure 2b,c). They both further had low polydispersity index (PDI) values which indicated a narrow size distribution and particles being relatively uniform in size. Transmission electron microscopy (TEM) images were acquired to reaffirm their spherical morphology (Figure S1). Subsequently, ζ- potential measurements were performed, showing ~ -38mV for DSPE-PEG@SP1. However, this decreased drastically for BSA@SP1 to ~ -6mV (Figure 2d, Figure S2). A plausible explanation could be attributed to the electrostatic screening effect by BSA molecules, effectively screening the original surface charge of the nanoparticles. Hydrodynamic diameter and zeta potential values were obtained for both DSPE-PEG@SP1 and BSA@SP1 for 1 week while stored at 4°C (Figure S3). Long-term colloidal stability of BSA@SP1 was evaluated at (i) 37°C (to mimic physiological temperature) and 10% plasma solution (to mimic biological milieu). They demonstrated no significant change in hydrodynamic diameter or PDI values, indicating their size stability and homogeneity (Figure S4). During this time, no visible precipitations were observed, indicating their excellent colloidal stability. Next, optical characterizations were conducted for both DSPE-PEG@SP1 and BSA@SP1 dispersed in PBS1x buffer, with a pH of 7.4. The absorption spectra revealed a prominent absorbance peak at 535nm for both nanoparticles, consistent with previous reports and

our bandgap measurements.[29] Upon excited at 605nm, both nanoparticles exhibited an emission peak at 820nm. However, BSA@SP1 displayed a significantly higher emission intensity compared to DSPE-PEG@SP1. To further investigate their fluorescence properties, we captured fluorescent images using the In Vivo Imaging System (IVIS) imager with excitation at 605nm and varying emission wavelength (680nm – 840nm). The fluorescence intensities demonstrated a similar trend for both nanoparticles (Figure 2g and Figure S5). Additionally, we acquired afterglow images using the bioluminescence mode of the IVIS imager. Remarkably, BSA@SP1 showed substantially higher afterglow luminescence compared to DSPE-PEG@SP1 (Figure 2h). The hydrophobic nature of PFODBT allows it to interact with BSA and become embedded within its hydrophobic domains. To investigate this interaction and its underlying effect on the improved optical behavior of PFODBT in the presence of BSA, preliminary molecular docking studies were conducted between PFODBT and BSA. As shown in Figure 2i-k, the amino acid residues of BSA exhibited strong hydrophobic interaction with PFODBT, particularly hydrophobic amino acids such as PRO-117 and LEU-178, which interacted with the alkyl side chains of PFODBT. Moreover, the aromatic ring of TYR-400 formed $\pi - \pi$ stacking interactions with the aromatic ring of PFODBT. These close interactions potentially limit the motion of PFODBT, thereby suppressing non-radiative decay and promoting the intersystem crossing process, ultimately enhancing the $^1O_2$ radical generation efficacy of PFODBT in the presence of an electron-rich environment of BSA. These factors culminate into enhanced afterglow brightness for BSA-coated PFODBT nanoparticles, compared to traditional encapsulation matrices like DSPE-PEG, which do not have any effects on the optical properties of PFODBT.

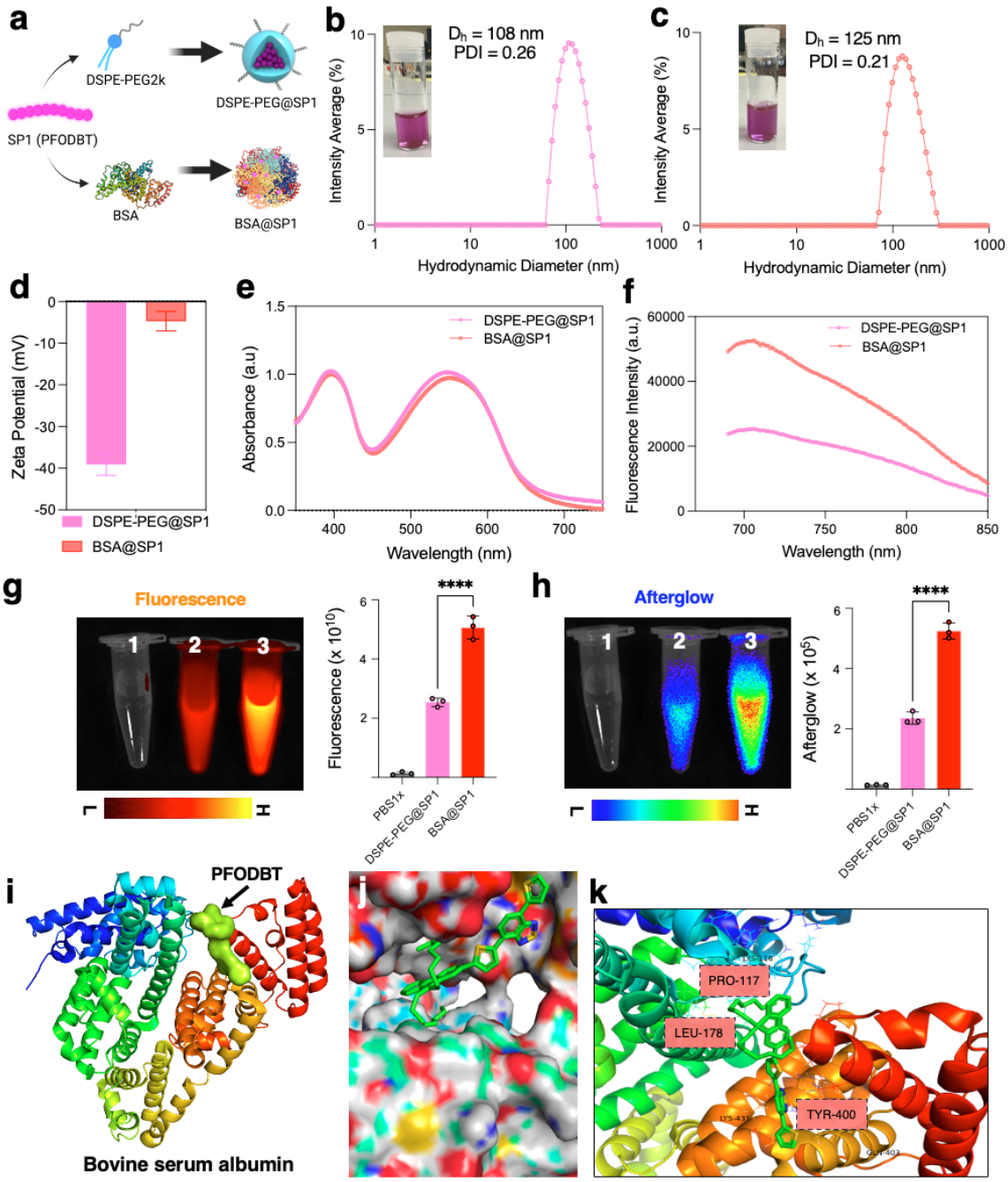

Figure 2. Physico-chemical and photophysical characterization of DSPE-PEG@SP1 and BSA@SP1. (a) Synthesis scheme of preparation of DSPE-PEG@SP1 and BSA@SP1 nanoparticles. Corresponding hydrodynamic diameter measurements from dynamic light scattering and insets showing the nanoparticle solutions for (b) DSPE-PEG@SP1, and (c) BSA@SP1, respectively. Zeta potential (d), UV-Vis-NIR absorption spectra (e), and

fluorescence emission spectra at 645nm excitation (f) of DSPE-PEG@SP1 and BSA@SP1. Fluorescence images (g) and afterglow images (h) were acquired using an IVIS imager and their corresponding intensities values were calculated with 1: PBS1x, 2: DSPE-PEG@SP1, 3: BSA@SP1. Molecular docking studies to evaluate the binding between PFODBT and BSA and analyzed with : (i) Receptor (BSA) as a cartoon and ligand (PFODBT) as a stick. (j) Receptor (BSA) as a surface and ligand (PFODBT) as a stick. (k) Interaction of the docked ligand (PFODBT) with the surrounding hydrophobic amino acid residues in BSA (highlighted in red).

Evaluation of Afterglow Emission Characteristics of BSA@SPs. Following an exhaustive physicochemical characterization and a thorough assessment of the long-term colloidal stability of BSA@SP1, our objective was to optimize the afterglow emission of BSA@SP1. We employed varying concentrations of BSA (0.66, 6.6 mg, and 13.2 mg/ mL) to coat the SP1 particles, forming BSA@SP1 nanoparticles. Subsequently, we quantified the afterglow emission intensities, which revealed the highest afterglow luminescence for the BSA@SP1 nanoparticles formed with 6.6 mg/ mL BSA (referred to as BSA66@SP1), while the emission from the BSA@SP1 nanoparticles formed with 13.2 mg/ mL BSA (referred to as BSA132@SP1) was comparable (Figure S6). Conversely, the lowest emission was observed for the complex formed with 0.66 mg/ mL BSA. Notably, as BSA132@SP1 exhibited a smaller dynamic light scattering (DLS) peak (~10 nm), likely due to excess BSA that could not be removed from centrifugation wash steps it posed a potential risk of instability for future experiments (Figure S7). Consequently, to ensure stability and reliability in subsequent measurements, we opted to use BSA66@SP1, further referred to as simply BSA@SP1. For our control nanoparticle, DSPE-PEG2k was used as a surfactant to coat SP1 using nanoprecipitation.

We first attempted to investigate how varying duration of light irradiation impacts the NIR afterglow luminescence emission of BSA@SP1. We observed that the intensity of the NIR afterglow from BSA@SP1 gradually increased with longer irradiation times, reaching its peak at 30 seconds and maintaining a similar signal for 60 seconds of irradiation (Figure 3b,e). In contrast, the fluorescence signal emitted by BSA@SP1 remained nearly constant regardless of the duration of irradiation (Figure 3f). This indicates that while the irradiation activates NIR afterglow luminescence for BSA@SP1, it does not affect their fluorescence emission. A similar trend was noted for DSPE-PEG@SP1, albeit with weaker afterglow luminescence and fluorescence emission signals compared to BSA@SP1 (Figure 3a,c,d). We aimed to investigate the persistence of NIR afterglow emission in BSA@SP1 once light irradiation ceased, as this feature could extend imaging time without compromising quality. Dynamic NIR afterglow images of BSA@SP1 revealed luminescence persisting for approximately 15 minutes post-irradiation (Figure 3g). In contrast, DSPE-PEG@SP1 exhibited weaker persistence, with luminescence fading within approximately 8 minutes. Subsequently, we attempted to investigate if BSA@SP1 could retain its afterglow luminescence across multiple cycles of irradiation. Such a characteristic would indicate their stability and durability, making them advantageous for prolonged observation for *in vivo* imaging without the need for repeated administration of the afterglow agent or re-irradiations, thereby minimizing perturbations to the in vivo system under investigation. BSA@SP1 was still bright after three rounds of irradiation (Figure 3i).

To elucidate the underlying mechanisms dictating the NIR afterglow luminescence in BSA@SP1, we first focused on whether heating could induce SP1/PFODBT to emit NIR afterglow. However, upon heating up to 60°C, we observed no discernible NIR afterglow

luminescence. In contrast, exposure of BSA@SP1 to 60 seconds of white light irradiation resulted in a notable enhancement of NIR afterglow intensity (Figure S8). Subsequently, we subjected BSA@SP1 to both hypoxic and normoxic environments and captured their respective afterglow luminescence images. Remarkably, under hypoxic conditions, the NIR afterglow luminescence of BSA@SP1 was significantly diminished compared to that under normoxic conditions (Figure S9). This observation implies that $^1O_2$ radicals might play a role in modulating the NIR afterglow luminescence of BSA@SP1.[31] Consequently, the logical progression was to investigate the generation of $^1O_2$ radicals, as earlier studies have linked their production to the afterglow phenomenon in PFODBT or SP1[32-34]. To assess the generation of $^1O_2$ radicals from SP1, we used a singlet oxygen sensor green (SOSG). After the white light irradiation was increased (1s to 60s), the fluorescence intensity of SOSG at 525nm increased by ~1.5x to 4x for BSA@SP1 as shown in Figure S10 suggesting the role the generation of $^1O_2$ radical plays afterglow luminescence. Interestingly, when exposed to white light irradiation, the fluorescence intensity of SOSG at 525nm was significantly higher for BSA@SP1 when compared to compared to DSPE-PEG@SP1 (Figure S11). A plausible explanation for this effect could be attributed to the role BSA serves by providing a rich electron microenvironment, acting as a substrate for $^1O_2$ radical generation.[28] Next, we investigated the correlation between NIR afterglow luminescence intensity and the generation of singlet oxygen in solution. As the irradiation time increased, we observed a substantial enhancement in the afterglow intensities of BSA@SP1 which aligned with a proportional increase in the fluorescence emission intensity of SOSG, indicating a corresponding rise in the amount of $^1O_2$ radicals (Figure S12). Remarkably, we discovered a strong correlation (Figure S13) between the yield of $^1O_2$ radicals and NIR afterglow luminescence intensity ($R^2 = 0.92$).

To gain deeper insights into the molecular mechanisms underlying the heightened generation of singlet oxygen ($^1O_2$) observed in BSA@SP1 and its subsequent afterglow luminescence, we conducted comparative experiments utilizing another SP dye, PCPDTBT, designated as SP2. By functionalizing SP2 with DSPE-PEG (DSPE-PEG@SP2) or BSA (BSA@SP2), we observed a similar augmentation in $^1O_2$ production. However, both DSPE-PEG@SP2 and BSA@SP2 exhibited no discernible afterglow luminescence (Figure S14-S15). This observation suggests a potential influence of the thiophene moieties present in SP1/PFODBT structures driving the afterglow luminescence, which is absent in SP2/PCPDTBT structures.

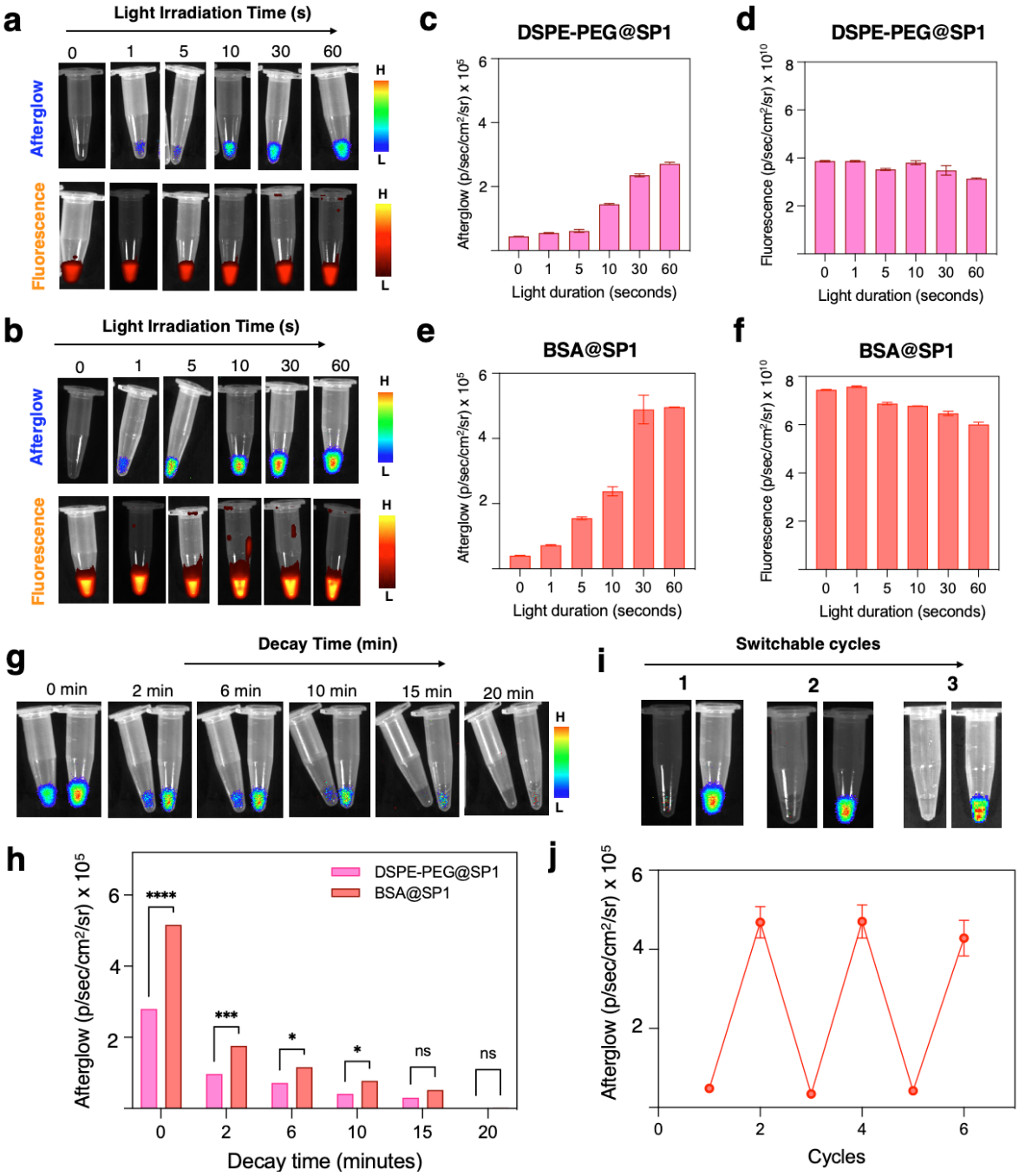

Figure 3. Evaluation of enhanced afterglow luminescence of BSA-coated PFODBT nanoparticles, i.e. BSA@SP1. Afterglow and fluorescence images of DSPE-PEG@SP1 (a) and BSA@SP1 (b) after receiving different light irradiation times and their corresponding afterglow (c, e) and fluorescent intensities (d, f) being calculated. Luminescence decay studies were conducted for DSPE-PEG@SP1 (left) and BSA@SP1 (right) and their afterglow images (g) and

intensities (h) were calculated after receiving irradiation. Afterglow images (i) and corresponding afterglow intensities for BSA@SP1 as a function of light irradiation cycles (j) where after each irradiation the nanoparticles were allowed to release the photons for 20 minutes.

***In Vitro* Cytotoxicity Assessment and Cellular Internalization of BSA@SP1 in Cancer Cell Lines.** After thoroughly characterizing BSA@SP1 and DSPE-PEG@SP1, we assessed their biocompatibility and ability to be internalized by 4T1 tumor cells *in vitro*. Both DSPE-PEG@SP1 and BSA@SP1 demonstrated minimal toxicity to the 4T1 cells, even at high concentrations of 100 µg/mL (Figure S16). To examine cellular internalization, we utilized flow cytometry to quantify uptake into 4T1 cells. Both DSPE-PEG@SP1 and BSA@SP1 exhibited increased uptake compared to the control (PBS 1x treatment). Particularly, BSA@SP1 demonstrated significantly higher cellular uptake (~27%) compared to DSPE-PEG@SP1 (~9.5%) (Figure S17). This trend may be attributed to the presence of secreted proteins acidic and rich in cysteine (SPARC) receptors that are highly expressed on metastatic tumor cells, such as 4T1, which are known to bind to albumin.[35] These receptors likely facilitate a selective endocytosis uptake mechanism for BSA@SP1. Further studies are underway in our laboratories to investigate the endocytosis uptake pathways of our BSA@SP1 in both SPARC-expressing and SPARC-non-expressing cancer cell lines. However, the details of these studies are not provided here.

***Ex Vivo* Porcine Tissue Permeation Profiling using Tumor-Mimicking Phantoms.** In evaluating the potential effectiveness of BSA@SP1 in surgical procedures, it is imperative to understand how their afterglow signals vary when tumors are deeply situated within normal

tissues. This understanding is crucial for guiding their future clinical applications. To investigate this behavior of BSA@SP1 across various tissue types, we utilized 3D tumor-mimicking phantom models using a methodology previously developed by us [29,30] comprising intralipids to simulate fat content (scattering component), hemoglobin to mimic blood vessels (absorption component), and tumor cells labeled with nanoparticles or solely nanoparticles at *in vivo* concentration levels (fluorescence component).[36] It offers distinct advantages over commonly adopted methods, such as utilizing intralipid solutions for simulation[31] because tumor-mimicking phantoms can more accurately replicate the optical properties of real tumors, including their scattering and absorption coefficients. As image-guided surgery relies on detecting NIR optical signals, typically from dye uptake, thus, employing phantoms that closely simulate these optical characteristics can yield more precise and realistic outcomes compared to simulations with intralipid solutions, especially when compared to actual *in vivo* imaging scenarios. Furthermore, these phantoms can be engineered to maintain their stability over time, ensuring consistent outcomes across experiments. In contrast, intralipid solutions may change their optical properties due to factors like temperature changes or particle aggregation, leading to variability in imaging outcomes.[38,39] Moreover, tumor phantoms can replicate the structural characteristics of tumors, including their dimensions, and morphology. By regulating the concentration of fluorophores within these phantoms, concentrations closer to those obtained *in vivo* mouse models can be achieved.

Here, we wanted to conduct tissue permeation profiling using BSA@SP1 tumor-mimicking phantoms and evaluate how their afterglow luminescence and fluorescence signals varied when covered with layers of porcine fat, muscle, and skin of varying thicknesses. The BSA@SP1 tumor-mimicking phantoms were prepared (Figure 4a) as described in the methods

section and upon covering with fat/muscle/skin of different depths, they were imaged using an IVIS imager under both fluorescence and bioluminescence imaging modes. We observed reductions in the fluorescence and afterglow tumor phantom-to-normal tissue (T/NT) ratios when various thicknesses of fat, muscle, and skin tissues were placed on top of the BSA@SP1 phantoms. The fluorescence T/NT ratios of BSA@SP1 phantoms experienced a significant drop from ~22 to ~6 when covered with a 2mm fat tissue (Figure 4c). This reduction further increased, reaching ~2 when a 4mm fat tissue, ~1.5 with 6mm, and eventually dropping to ~1 with the addition of a 10mm fat tissue addition (Figure 4c). As anticipated, the afterglow T/NT ratios of BSA@SP1 phantoms were higher than fluorescence T/NT ratios due to the former's background signal compared to fluorescence. The afterglow T/NT ratios of BSA@SP1 decreased from ~45 to ~16 when covered with a 2mm layer of fat tissue. This reduction increased progressively, reaching ~9 when a 4mm fat tissue, ~6.5 with 6mm, and eventually dropping to ~5.4 for 8mm fat tissue covering, and 4.5 with the addition of a 10mm fat tissue layer. Remarkably, these T/NT ratios remained above the Rose criterion of 5,[40-42] even up to 8mm depth, underscoring the promising potential of afterglow luminescence in deep tissue imaging. A similar trend was observed for afterglow vs. fluorescence images for BSA@SP1 phantoms when covered with sequential 2mm tissue slices of porcine muscles where the T/NT ratios (>5) for afterglow were significantly higher than fluorescence for tissue slices of till ~6mm (Figure 4g). Finally, to investigate the signal penetration for BSA@SPNs on the epidermis, we placed porcine skin on top of BSA@SP1 phantoms. We observed again a significant reduction in fluorescent signals, whereas afterglow signals despite dropping had a substantially higher T/NT ratio when compared to fluorescence signals in skin (Figure 4e). The loss of fluorescence signal through the skin or other tissue types is not a significant concern, especially as most image-guided surgeries

are open surgeries. However, having the advantage of deeper penetration provided by afterglow luminescence can enable us to locate the precise location for buried tumor lesions surrounding fat and muscle tissues. We would like to highlight a key difference between our study and recent ones on evaluating the depth penetration of afterglow luminescence. While many seminal studies have predominantly used nanoparticle solutions,[12,43] we opted for 3D tumor-mimicking phantoms. This decision introduced us to certain challenges, particularly intralipid and hemoglobin, which could potentially dampen afterglow luminescence signals. However, these factors were not encountered in the studies using nanoparticle solutions for depth penetration. Additionally, another contributing factor could be the concentration difference between our samples and those in existing literature.[12,43] We maintained a final concentration of ~10 μg/mL of BSA@SPs in our phantoms, whereas studies often utilized concentrations approximately ~ten-fold higher (~60-100μg/mL) for their depth penetration studies.[12,43] This disparity in experimental setups might explain why some studies achieved depth penetrations of approximately 10-30mm for afterglow luminescence, whereas our results ranged from 8-10mm. Overall, our findings demonstrate that by conducting depth penetration studies under more realistic *in vivo* conditions, we consistently observed stronger afterglow luminescence signals at deeper tissue depths in comparison to fluorescence signals.

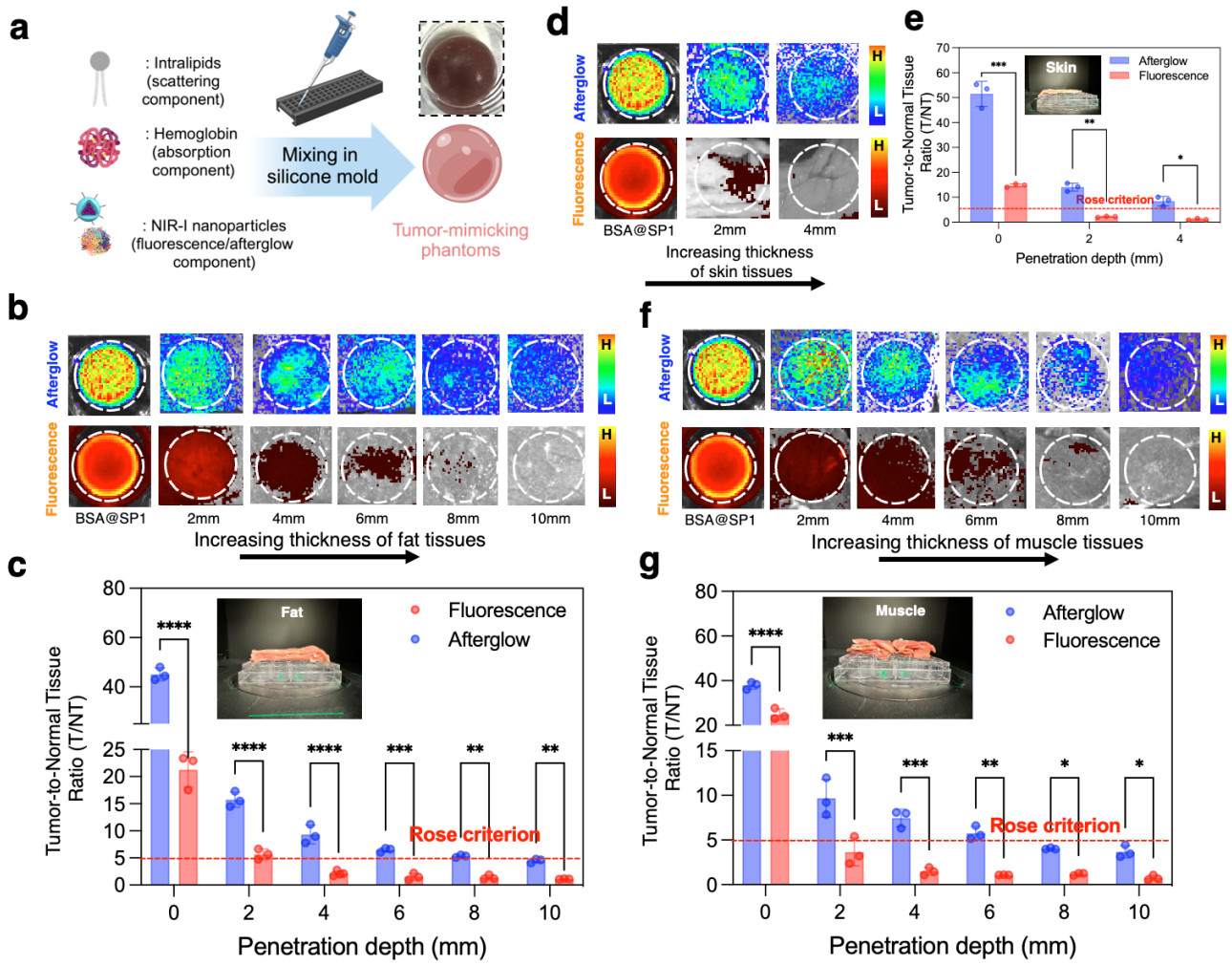

Figure 4. *Ex vivo* imaging of tissue penetration and signal-to-background ratios of BSA@SP1 afterglow luminescence and fluorescence. (a) Schematic process showing the preparation process of tumor-mimicking phantoms and inset showing the picture of a representative as-prepared phantom. Afterglow and fluorescence images of tumor-mimicking phantoms covered with increasing width of tissue slices of (b) fat, (d) skin, and (f) muscle. The corresponding tumor phantom-to-normal tissue (T/NT) ratios for both afterglow and fluorescence were plotted and compared for (c) fat, (e) skin, and (g) muscle.

Aterglow-guided Thoracic Surgery Simulations on *Ex Vivo* Porcine Lungs. Inspired by the superior performance of BSA@SP1 tumor-mimicking phantoms, which exhibit robust T/NT signal ratios in afterglow imaging, we explored their potential applications in afterglow-guided surgery. Our investigation utilized *ex vivo* porcine lungs as experimental models, with strategically implanted tumor-mimicking phantoms at various locations to simulate diverse scenarios akin to image-guided thoracic surgery. Three selected locations (Figure 5a) were chosen to simulate different thoracic surgery scenarios: on the surface of the right inferior lobe (location #1), on the posterior side of the left inferior lobe (location #2), and between the trachea and the right superior lobe (location #3). Subsequently, these locations were imaged using both fluorescence and afterglow imaging *via* an IVIS imager. At location #1, characterized by a surface-level tumor phantom placement, we observed strong fluorescence and afterglow signals. Despite higher background signals from surrounding tissues in fluorescence imaging, the fluorescence signal from the tumor phantom could be discerned (Figure 5b, location #1). The tissue background signal in the afterglow imaging was minimal, allowing only afterglow luminescence signals from the tumor phantoms. In contrast, at location #2, where the tumor phantom was buried deeper within the left inferior lobe, the fluorescence signal diminished significantly, while tissue autofluorescence continued to pose interference. Conversely, afterglow luminescence imaging at this location showed a strong signal with reduced interferences from surrounding tissues, as anticipated (Figure 5b, location #2). Lastly, location#3 was designed to present the most challenging scenario due to its anatomical accessibility constraints. Clear imaging signals from tumors at such locations could allow the planning of more efficient surgical intervention strategies. Afterglow imaging, with its lower background signal from surrounding tissues, provided a more precise localization of the tumor phantoms compared to fluorescence

imaging (Figure 5b, location #3). At these three locations, we calculated the T/NT ratios, which were superior in afterglow imaging compared to fluorescence imaging, even at location #3 (Figure 5c). Moreover, these ratios were significantly higher than the Rose criterion. These findings underscore the potential of afterglow imaging, particularly in scenarios where fluorescence imaging encounters limitations due to tissue autofluorescence and depth of tumor localization. This preliminary *ex vivo* studies further highlights the promising role of afterglow-guided surgery in enhancing surgical precision and outcomes in thoracic procedures.

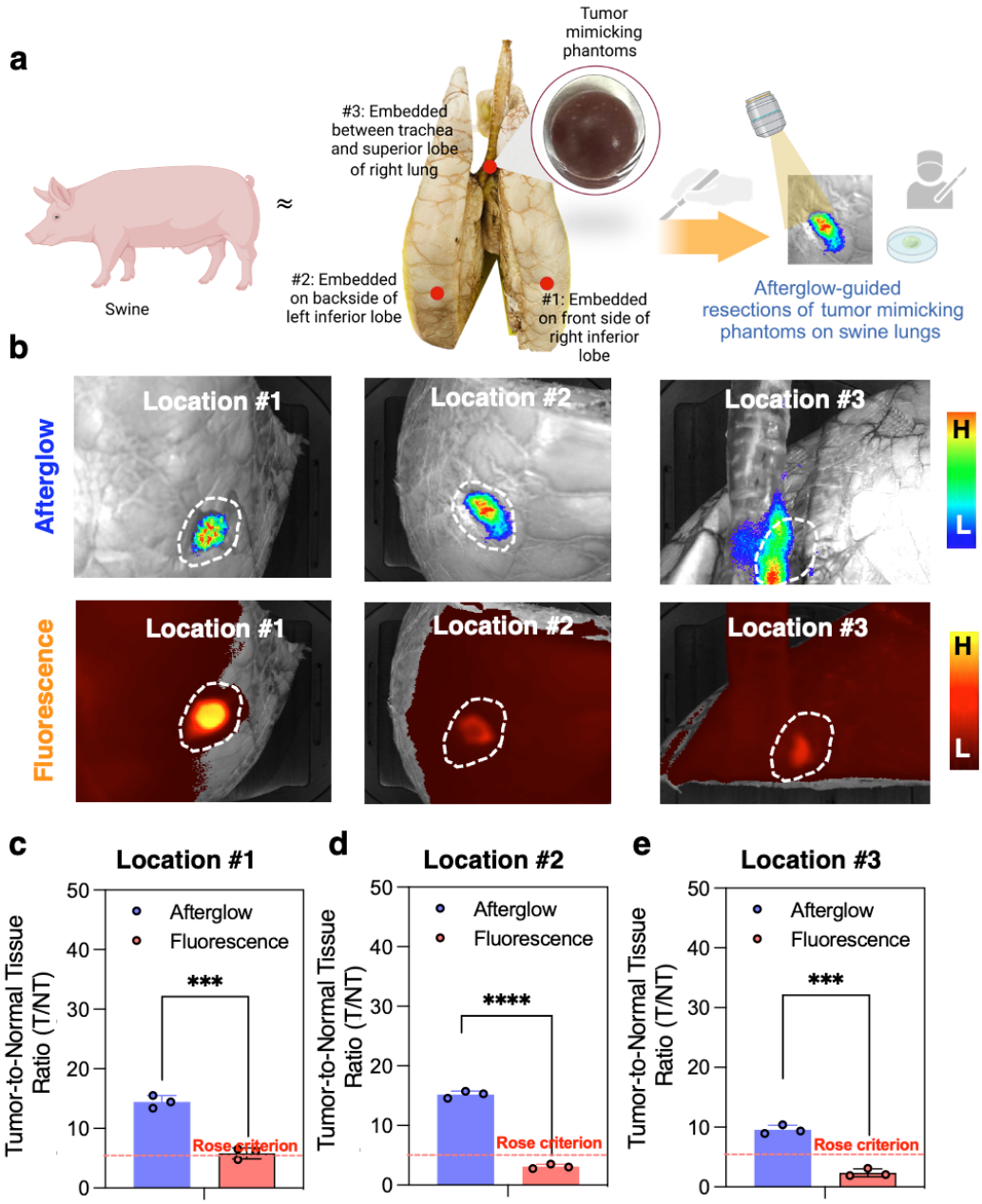

Figure 5. Afterglow luminescence-guided surgery using BSA@SP1 on swine lungs embedded with tumor cell-mimicking phantoms. (a) Schematic process showing embedding of tumor-mimicking phantoms on *ex vivo* porcine lungs at different locations (#1, #2, #3). (b) Afterglow and fluorescence imaging of these three different locations using an IVIS Imager, and (c) corresponding T/NT ratios were measured.

CONCLUSION.

In this report, we have introduced a novel repurposing technique using a BSA coating that enhances the suboptimal afterglow brightness of existing NIR-I afterglow luminescence materials, using a semiconducting polymer (PFODBT/SP1) as a representative example. Through this approach, BSA@SP1 demonstrated a ~3-fold amplification of the afterglow luminescence signal compared to polymer-lipid-coated PFODBT. Our comprehensive analysis, including molecule docking, physicochemical characterization, and optical assessments, highlights BSA@SP1's superior afterglow properties, cyclic afterglow behavior, long-term colloidal stability, and biocompatibility. Furthermore, we validated the efficacy of BSA@SP1 in aiding surgical interventions using *ex vivo* tumor-mimicking phantom models. Our porcine tissue permeation profiling studies revealed that afterglow signals, with their high T/NT ratios, outperformed fluorescence signals. We also simulated thoracic surgeries on *ex vivo* porcine lungs with implanted tumor-mimicking phantoms, showcasing the advantages of afterglow luminescence over fluorescence imaging for surgical resections. Thus, our protein-based repurposing strategy holds promise for enhancing the brightness of existing and upcoming NIR-I afterglow materials, making them valuable tools for image-guided surgical interventions.

METHODS.

Materials. All materials were purchased from Sigma-Aldrich and used without any modifications unless stated separately. Pork skin, fat, and muscle tissues were acquired from local grocery stores. Dry-preserved porcine lung was purchased from Nasco Education. The SOSG test kit was received as a complementary gift from Lumiprobe USA.

Preparation of DSPE-PEG@SP1. For preparing DSPE-PEG@SP1, 0.5 mg of SP1/PFODBT were co-dissolved in 2 mL of THF with 10 mg of surfactant, DSPE-PEG2K. This was followed by a dropwise addition of 8mL PBS1x solution in a 20mL vial under probe sonication for 4 minutes. THF was subsequently evaporated from the solution by stirring at 450 rpm at room temperature overnight. The mixture solution was ultrafiltered at 4500 rpm for 10 minutes and then washed three times with PBS1x to remove any excess precursors. The final product (DSPE-PEG@SP1) was collected and stored at 4 °C.

Preparation of BSA@SP1. 0.5 mg of SP1/PFODBT were dissolved in 2 mL of THF. 66 mg of BSA was dissolved in 10 mL of PBSx1 in a separate vial and heated to approximately 37°C to ensure homogeneity. SP1 solution was then added dropwise to 8mL of BSA-PBS1x solution and sonicated for 4 minutes. THF was subsequently evaporated overnight by stirring at 450 rpm. The mixed solution was ultrafiltered at 4500 rpm for 10 minutes three times and then washed three times with PBS1x to remove any excess precursors or unreacted BSA. The final product (BSA@SP1) was collected and stored at 4 °C.

Preparation of DSPE-PEG@SP2. For preparing DSPE-PEG@SP2, 0.5 mg of SP2/PCPDTBT were co-dissolved in 2 mL of THF with 10 mg of surfactant, DSPE-PEG2K. This was followed

by a dropwise addition of 8mL PBS1x solution in a 20mL vial under probe sonication for 4 minutes. THF was subsequently evaporated from the solution by stirring at 450 rpm at room temperature overnight. The mixture solution was ultrafiltered at 4500 rpm for 10 minutes and then washed three times with PBS1x to remove any excess precursors. The final product (DSPE-PEG@SP2) was collected and stored at 4 °C.

Preparation of BSA@SP2 0.5 mg of SP2/PCPDTBT was dissolved in 2 mL of THF. 66 mg of BSA was dissolved in 10 mL of PBSx1 in a separate vial and heated to approximately 37°C to ensure homogeneity. SP2 solution was then added dropwise to 8mL of BSA-PBS1x solution and sonicated for 4 minutes. THF was subsequently evaporated overnight by stirring at 450 rpm. The mixed solution was ultrafiltered at 4500 rpm for 10 minutes three times and then washed three times with PBS1x to remove any excess precursors or unreacted BSA. The final product (BSA@SP2) was collected and stored at 4°C.

Physicochemical and Optical Characterization. Dynamic light scattering (DLS) measurements were conducted to measure the hydrodynamic diameter of nanoparticles using a Litesizer DLS 700 Particle Analyzer instrument (Anton Paar). For each measurement, 50 µL of nanoparticle solution and 950 µL of PBSx1 were used. ζ- Potential measurements were also taken using the Litesizer DLS 700 Particle Analyzer instrument (Anton Paar). Ultraviolet-visible (UV-VIS) absorbance was recorded on a Genesys 30 Visible Spectrophotometer (ThermoFisher Scientific). The absorption spectra were collected at an interval of 1nm scanning from 325nm to 1100nm. Fluorescence spectra were collected on an RF-6000 Spectro Fluorophotometer

(Shimadzu). The emission spectra were collected at an interval of 1nm scanning from 690nm to 800nm.

Transmission Electron Microscopy (TEM) Imaging. A small amount of the nanoparticle solution containing either DSPE-PEG@SP1 or BSA@SP1 was dropped onto a glow-discharged, carbon-coated TEM grid and incubated for 5-10 minutes. Excess liquid was removed, and samples were left to completely dry overnight in a desiccation chamber. All samples were imaged using a JOEL JEM-2100 Cryo transmission electron microscope at 200 kV.

Colloidal Stability of BSA@SP1 in a Biological Milieu. The hydrodynamic diameter, PDI, and zeta potential values of BSA@SP1 in PBS1x and 10% plasma solution were measured over time (days 1 - 7). All samples were maintained at 37°C, oscillating in a Solaris 2000 orbital shaker (ThermoFisher Scientific), and after each time point, the hydrodynamic diameter, PDI, and zeta potential values were recorded using Litesizer7000 (Anton Parr).

Fluorescence and Afterglow Imaging using IVIS Imager. Fluorescence and afterglow imaging of nanoparticles (DSPE-PEG@SP1 or BSA@SP1) were conducted using an IVIS imager. ~200 μL solutions of either DSPE-PEG@SP1 or BSA@SP1 were prepared in centrifuge tubes for both fluorescence imaging and afterglow imaging. For fluorescence imaging, the fluorescence was acquired at an excitation wavelength of 605nm, and emission wavelength of 720nm. For afterglow imaging, the samples were first irradiated for different durations using a 1000-lumen LED white-light source. Subsequently, they were imaged in the IVIS imager under the open filter setting and bioluminescence imaging mode.

Molecular Docking Calculations. The 3D structure of Bovine Serum Albumin (BSA) (PDB ID: 4F5S) was chosen as the receptor for molecular docking, employing UCF Chimera software. The receptor input file and the ligand structure of PFODBT were prepared separately using Avogadro software, saving them in PDB format for docking. Additionally, specific parameters for the active pocket were defined for the grid box in vina1.2.3 program: x=42.35, y=32.77, z=98.61, with dimensions x=131.07, y=83.35, z=117.02. Default settings were applied for exhaustiveness=8, number of modes=9, and energy range=3 during docking. Post-generation of the requisite files, default parameters were retained for the PFODBT molecule. Subsequently, the best scoring conformation (with an energy of -6.1 kcal/mol), was identified and merged with the protein, saved as a complex, and subjected to analysis using Pymol to elucidate the small molecule-receptor mode of action. In Pymol software, the final pdbqt file of the ligand was combined with the receptor's final pdb file. Employing the 'ligand site' preset mode, all amino acid residues interacting with the ligand were selected and labeled. Furthermore, utilizing the 'measurement wizard', the distances between the ligand and receptor amino acids were calculated in Angstrom units.

Singlet Oxygen Detection. Singlet oxygen sensor green (SOSG) was used to evaluate the singlet oxygen generation by PFODBT/SP1 in DSPE-PEG@SP1 and BSA@SP1 after light irradiation. Both nanoparticles (~10 μg/mL) were mixed with SOSG (final concentration of 5 μM) and irradiated with white light for a series of different times. Subsequently, the fluorescence intensity of SOSG was measured at 505nm of excitation and the singlet oxygen generation was quantified by comparing the SOSG fluorescence emission at 525nm.[44]

MTT Assay of DSPE-PEG@SP1 and BSA@SP1. The cytotoxic effect of the nanoparticles in 4T1 cells was investigated using an MTT assay established previously.[45,46]

***In Vitro* Cellular Uptake Experiments.** Flow cytometry was conducted to quantify cellular uptake. 4T1 cancer cells were incubated with DSPE-PEG@SP1 and BSA@SP1 at a concentration of 50 μg/mL for 8 hours. Subsequently, the treated cells were washed with PBS 1x, trypsinized, collected, and resuspended in a 1% FBS in PBS solution for cellular uptake analysis using a BD LSRFortessa.

Tumor Cell-Mimicking Phantom Models Preparation. Tumor cell-mimicking phantoms were prepared using a silicone mold. These phantoms consist of a mixture containing 720 mg type-A gelatin, 150 mg human hemoglobin, 900 μL of intralipid 20%, and 17.1 mL of PBS1x. Firstly, the gelatin is activated in the PBS1x at 60°C with stirring at 950 rpm for 30 minutes. Once the gelatin is activated, the biological components are added to the solution. The vial is inverted, vortexed, and mixed at 60°C with stirring at 950 rpm for an additional 10 minutes. Next, the mold wells are filled with 500 μL of either 50 μg/mL of DSPE-PEG@PFODBT or BSA@PFODBT and 1.5 mL of the phantom stock solution. For the control phantom, 500 μL of PBS1x is used instead of either DSPE-PEG@PFODBT or BSA@PFODBT solution. The mold is placed in the freezer, and the tumor phantoms are allowed to solidify for a minimum of one hour. Each tumor phantom created using the mold has a uniform total volume of 2 mL for every replicate batch.

***Ex Vivo* Porcine Tissue Penetration Experiments.** To replicate the properties of human skin, muscle, and fat tissues, three distinct porcine tissue samples were utilized. Skin tissue was simulated using a slice of pork belly, chosen for its similarity in texture and composition. Pork tenderloin, known for its low-fat content relative to other swine tissues, served as simulated muscle tissues. Fat (adipose) tissue was simulated using a fatty cut of pork chop. All tissues were procured from local supermarkets and uniformly sliced to a thickness of 2mm using a deli meat slicer (Anescva Premium Slicer Machine) in the laboratory.

To accommodate for the variability in tumor depth, the tissue slices were stacked accordingly. Skin tissues were stacked up to a depth of 4 mm, representing the maximum thickness observed in human skin. Muscle and fat tissues were stacked at various depths at which tumors may occur, ranging from surface-level to buried tumor lesions. Tumor-mimicking phantoms were prepared using a solution of 720 mg type A gelatin, 17.1 mL of PBS1x, 150 mg human hemoglobin, and 900 µL of intralipid 20%. In a silicone mold, a combination of 500 µL of 1X PBS (control) and either 500 µL of 50 µg/mL DSPE-PEG@PFODT or BSA@PFODBT were added, along with 1.5 mL of phantom stock solution, was used to create the tumor-mimicking phantoms for imaging. These phantoms were then placed in a 12-well plate for further analysis. Fluorescence imaging was conducted in the IVIS imager, at an excitation filter of 605 nm and an emission filter of 720 nm for both DSPE-PEG@PFODBT and BSA@PFODBT. For afterglow imaging, before the addition of each layer of tissue, all tumor phantoms were irradiated for 60 seconds with a 1000-lumen LED white-light source.

Afterglow-Guided Surgery on *Ex Vivo* Porcine Lung. A dry-preserved porcine lung was purchased from Nasco Education™, USA, and used for conducting simulated image-guided surgery. To optimize imaging using an IVIS imager for afterglow and fluorescence, the porcine lung sample underwent sectioning. Specifically, we focused on sections from the lower portions of the left and right posterior lobes of the lung, as well as an upper section of the inferior lobe, which included a portion of the trachea. These sections were chosen to replicate common sites for thoracic surgery. Tumor-mimicking phantoms were prepared exclusively by pouring a combination of 500 μL phantom solution (720 mg type A gelatin and 17.1 mL of PBS1x) and 500 μL of 50 μg/mL BSA@PFODBT in each silicon mold. The phantoms were then embedded in the three selected locations of the lung: (i) embedded 0.5 mm into the ventral surface of the right inferior lobe, (ii) embedded 5mm below the ventral surface of the right inferior lobe, and (iii) embedded between the surface of the trachea and the right superior lobe. Before each round of imaging using the IVIS in the bioluminescence setting (for afterglow), the tumor phantoms were irradiated with a 1000-lumen LED white-light source for 60 seconds. For fluorescence imaging, the excitation wavelength of BSA@PFODBT was selected as 605 nm and the emission wavelength was selected as 720 nm.

Statistical Analysis. GraphPad Prism was used for statistical analysis throughout this work. Statistical comparisons were made by unpaired Student's *t*-test (between two groups) and one-way ANOVA (for multiple comparisons) with Tukey's post-hoc analysis. P value < 0.05 was considered statistically significant. Quantitative data were shown as mean ± standard deviation (SD).

ASSOCIATED CONTENT

Supporting Information. A listing of the contents of each file supplied as Supporting Information should be included. For instructions on what should be included in the Supporting Information as well as how to prepare this material for publication, refer to the journal's Instructions for Authors.

The following files are available free of charge.

brief description (file type, i.e., PDF)

brief description (file type, i.e., PDF)

AUTHOR INFORMATION

Corresponding Author

*indrajit.srivastava@ttu.edu

Author Contributions

I.S. conceived the idea and designed all the experiments. N.B., K.N., I.V., and I.S. performed all the experiments. A.H. performed molecular docking studies. I.S. wrote the first draft of the manuscript with edits from all the authors. All authors have approved the final version of the manuscript. ‡ N.B. and K.N. contributed equally.

ACKNOWLEDGMENT

I.S. acknowledges the Edward E. Whitacre Jr. College of Engineering and Texas Tech University for research support. All graphics in this paper were made in Biorender.

REFERENCES

(1) DeSantis, C. E.; Lin, C. C.; Mariotto, A. B.; Siegel, R. L.; Stein, K. D.; Kramer, J. L.; Alteri, R.; Robbins, A. S.; Jemal, A. Cancer Treatment and Survivorship Statistics, 2014. *CA. Cancer J. Clin.* **2014**, *64* (4), 252–271.

(2) Pilewskie, M.; Morrow, M. Margins in Breast Cancer: How Much Is Enough? *Cancer* **2018**, *124* (7), 1335–1341.

(3) Abraham, S. C.; Fox, K.; Fraker, D.; Solin, L.; Reynolds, C. Sampling of Grossly Benign Breast Reexcisions: A Multidisciplinary Approach to Assessing Adequacy. *Am. J. Surg. Pathol.* **1999**, *23* (3), 316–322.
(4) Madajewski, B.; Judy, B. F.; Mouchli, A.; Kapoor, V.; Holt, D.; Wang, M. D.; Nie, S.; Singhal, S. Intraoperative Near-Infrared Imaging of Surgical Wounds after Tumor Resections Can Detect Residual Disease. *Clin. Cancer Res.* **2012**, *18* (20), 5741–5751.
(5) Mondal, S.; Tsen, S.; Achilefu, S. Head-Mounted Devices for Noninvasive Cancer Imaging and Intraoperative Image-Guided Surgery. *Adv. Func. Mater.* **2020**, 30, 2000185.
(6) Kurbegovic, S.; Juhl, K.; Chen, H.; Qu, C.; Ding, B.; Leth, J.; Drzewiecki, K.; Kjaer, A.; Cheng, Z. Molecular Targeted NIR-II Probe for Image-Guided Brain Tumor Surgery. *Bioconjugate Chem.* **2018**, 29 (11), 3833-3840.
(7) Vahrmeijer, A. L.; Hutteman, M.; van der Vorst, J. R.; van de Velde, C. J. H.; Frangioni, J. V. Image-Guided Cancer Surgery Using Near-Infrared Fluorescence. *Nat. Rev. Clin. Oncol.* **2013**, *10* (9), 507–518.
(8) Miwa, S.; Hiroshima, Y.; Yano, S.; Zhang, Y.; Matsumoto, Y.; Uehara, F.; Yamamoto, M.; Kimura, H.; Hayashi, K.; Tsuchiya, H.; Hoffman, R. M. Fluorescence-Guided Surgery Improves Outcome in an Orthotopic Osteosarcoma Nude-Mouse Model. *J. Orthop. Res. Off. Publ. Orthop. Res. Soc.* **2014**, *32* (12), 1596–1601.
(9) Fujita, T. Reality or Dream of Fluorescence-Guided Pancreatic Cancer Surgery? *J. Am. Coll. Surg.* **2012**, *215* (4), 591.
(10) Xu, G.; Yan, Q.; Lv, X.; Zhu, Y.; Xin, K.; Shi, B.; Wang, R.; Chen, J.; Gao, W.; Shi, P.; Fan, C.; Zhao, C.; Tian, H. Imaging of Colorectal Cancers Using Activable Nanoprobes with Second Near-Infrared Window Emission. *Angew. Chem.* **2018,** 130, 3688-3692.
(11) Yang, R.; Lou, K.; Wang, P.; Gao, Y.; Zhang, Y.; Chen, M.; Huang, W.; Zhang, G. Surgical Navigation for Malignancies Guided by Near-Infrared-II Fluorescence Imaging. *Small Methods* **2021**, 5, 2001066.
(12) Miao, Q.; Xie, C.; Zhen, X.; Lyu, Y.; Duan, H.; Liu, X.; Jokerst, J. V.; Pu, K. Molecular Afterglow Imaging with Bright, Biodegradable Polymer Nanoparticles. *Nat. Biotechnol.* **2017**, *35* (11), 1102–1110.
(13) Xu, C.; Huang, J.; Jiang, Y.; He, S.; Zhang, C.; Pu, K. Nanoparticles with Ultrasound-Induced Afterglow Luminescence for Tumour-Specific Theranostics. *Nat. Biomed. Eng.* **2023**, *7* (3), 298–312.
(14) Chen, W.; Zhang, Y.; Li, Q.; Jiang, Y.; Zhou, H.; Liu, Y.; Miao, Q.; Gao, M. Near-Infrared Afterglow Luminescence of Chlorin Nanoparticles for Ultrasensitive In Vivo Imaging. *J. Am. Chem. Soc.* **2022**, *144* (15), 6719–6726.
(15) Li, Y.; He, D.; Zheng, Q.; Tang, R.; Wan, Q.; Tang, B.; Wang, Z. Single Component Photochemical Afterglow Near-Infrared Luminescent Nano-Photosensitizers: Bioimaging and Photodynamic Therapy. *Adv. Healthcare Mater.* **2024,** 2304392, 1-9.
(16) Yao, H.; Zhang, Y.; Wang, G.; Li, J.; Huang, J.; Wang, X.; Zhang, Z.; Chen, L.; Pan, Z.; Zhang, K. TADF-Type Organic Afterglow Nanoparticles with Temperature and Oxygen Dual-Responsive Property for Bimodal Sensing. *ACS Appl. Nano Mater.* **2023**, *6* (16), 15138–15146.
(17) Ni, X.; Zhang, X.; Duan, X.; Zheng, H.-L.; Xue, X.-S.; Ding, D. Near-Infrared Afterglow Luminescent Aggregation-Induced Emission Dots with Ultrahigh Tumor-to-Liver Signal Ratio for Promoted Image-Guided Cancer Surgery. *Nano Lett.* **2019**, *19* (1), 318–330.

(18) Chen, C.; Zhang, X.; Gao, Z.; Feng, G.; Ding, D. Preparation of AIEgen-based Near-Infrared Afterglow Luminescence Nanoprobes for Tumor Imaging and Image-guided Tumor Resection. *Nat. Protoc.* **2024**.
(19) Qu, R.; He, D.; Wu, M.; Li, H.; Liu, S.; Jiang, J.; Wang, X.; Li, R.; Wang, S.; Jiang, X.; Zhen, X. Afterglow/Photothermal Bifunctional Polymeric Nanoparticles for Precise Post Breast-Conserving Surgery Adjuvant Therapy and Early Recurrence Theranostic. *Nano Lett.* **2023**, 23 (10), 4216-4225.
(20) Liu, S.; Tian, Y.; Ye, D. Seeing Deeper via Radio Afterglow Imaging. *Chem. Biomed. Imaging* **2024**, 2, 1-3.
(21) Anjong, T.; Choi, H.; Yoo, J.; Bak, Y.; Cho, Y.; Kim, D.; Lee, S.; Lee, K.; Kim, B.; Kim, S. Multifunction-Harnessed Afterglow Nanosensor for Molecular Imaging of Acute Kidney Injury In Vivo. *Small* **2022**, 18, 2200245.
(22) Liu, Z.; Chen, X. Simple Bioconjugate Chemistry serves great clinical advances: albumin as a versatile platform for Diagnosis and Precision Therapy. *Chem. Soc. Rev.* **2016**, 45, 1432-1456.
(23) Zhu S, Hu Z, Tian R, Yung BC, Yang Q, Zhao S, et al. Repurposing Cyanine NIR-I Dyes Accelerates Clinical Translation of Near-Infrared-II (NIR-II) Bioimaging. Adv Mater. 2018: e1802546.
(24) Gao S, Wei G, Zhang S, Zheng B, Xu J, Chen G, et al. Albumin tailoring Fluorescence and Photothermal Conversion effect of Near-infrared-II Fluorophore with Aggregation-induced Emission Characteristics. *Nat Commun.* 2019; 10: 2206.
(25) Bai, L.; Hu, Z.; Han, T.; Wang, Y.; Xu, J.; Jiang, G. et al. Super-stable Cyanine@Albumin Fluorophore for Enhanced NIR-II Bioimaging. *Theranostics* **2022**, 12 (10), 4536-4547.
(26) Du, B.; Qu, C.; Qian, K.; Ren, Y.; Li, Y.; Cui, X. et al. An IR820 Dye-Protein Complex for Second Near-Infrared Window and Photoacoustic Imaging. Adv Opt Mater. 2019, 8, 1901471.
(27) Tian, R.; Zeng, Q.; Zhu, S.; Lau, J.; Chandra, S.; Ertsey, R. et al. Albumin-Chaperone Cynanine Dyes yields Superbright NIR-II Fluorophore with Enhanced Pharmacokinetics. *Sci Adv.* **2019**, 5: eaaw0672.
(28) Li, Y.; Zhang, D.; Yu, Y.; Zhang, L.; Li, L.; Shi, L.; Feng, G.; Tang, B. Z. A Cascade Strategy Boosting Hydroxyl Radical Generation with Aggregation-Induced Emission Photosensitizers-Albumin Complex for Photodynamic Therapy. *ACS Nano* **2023**, *17* (17), 16993–17003.
(29) Srivastava, I., Lew, B., Wang, Y., Blair, S., George, M. B., Hajek, B. S., Bangru, S., Pandit, S., Wang, Z., Ludwig, J., Flatt, K., Gruebele, M., Nie, S., Gruev, V. Cell-Membrane Coated Nanoparticles for Tumor Delineation and Qualitative Estimation of Cancer Biomarkers at Single Wavelength Excitation in Murine and Phantom Models. *ACS Nano* **2023**, 17 (9), 8465-8482.
(30) Srivastava, I., Xue, R., Huang, H.-K., Wang, Z., Jones, J., Vasquez, I., Pandit, S., Lin, L., Zhao, S., Flatt, K., Gruev, V., Chen, Y.-S., Nie, S. Biomimetic-Membrane-Protected Plasmonic Nanostructures as Dual-Modality Contrast Agents for Correlated Surface-Enhanced Raman Scattering and Photoacoustic Detection of Hidden Tumor Lesions. *ACS Appl. Mater. Interfaces* **2024**, 16, 7, 8554.
(31) Wang, Y., Song, G., Liao, S., Qin, Q., Zhao, Y., Shi, L., Guan, K., Gong, X., Wang, P., Yin, X., Chen, Q., Zhang, X.-B. Cyclic Amplification of the Afterglow Luminescent

Nanoreporter Enables the Prediction of Anti-cancer Efficiency. *Angew. Chem. Int. Ed.* **2021**, 60, 19779-19789.
(32) Lee, D.; Khaja, S.; Velasquez-Castano, J. C.; Dasari, M.; Sun, C.; Petros, J.; Taylor, W. R.; Murthy, N. In Vivo Imaging of Hydrogen Peroxide with Chemiluminescent Nanoparticles. *Nat. Mater.* **2007**, *6* (10), 765–769.
(33) Wang, Y.; Shi, L.; Ye, Z.; Guan, K.; Teng, L.; Wu, J.; Yin, X.; Song, G.; Zhang, X.-B. Reactive Oxygen Correlated Chemiluminescent Imaging of a Semiconducting Polymer Nanoplatform for Monitoring Chemodynamic Therapy. *Nano Lett.* **2020**, *20* (1), 176–183.
(34) Liao, S.; Wang, Y.; Li, Z.; Zhang, Y.; Yin, X.; Huan, S.; Zhang, X.-B.; Liu, S.; Song, G. A Novel Afterglow Nanoreporter for Monitoring Cancer Therapy. *Theranostics* **2022**, *12* (16), 6883–6897.
(35) Xu, Y.; Yang, C.; Wu, Y.; Jiang, W.; Cheng, Q.; Yan, L.; Chen, K.; Wang, Y. In Situ Albumin-Hitchhiking NIR-II Probes for Accurate Detection of Micrometastases. *Nano Lett.* **2023**, *23* (12), 5731–5737.
(36) Hacker, L.; Wabnitz, H.; Pifferi, A.; Pfefer, T. J.; Pogue, B. W.; Bohndiek, S. E. Criteria for the Design of Tissue-Mimicking Phantoms for the Standardization of Biophotonic Instrumentation. *Nat. Biomed. Eng.* **2022**, *6* (5), 541–558.
(37) Flock, S. T.; Jacques, S. L.; Wilson, B. C.; Star, W. M.; van Gemert, M. J. Optical Properties of Intralipid: A Phantom Medium for Light Propagation Studies. *Lasers Surg. Med.* **1992**, *12* (5), 510–519.
(38) Ninni, P. D.; Martelli, F.; Zaccanti, G. Intralipid: Towards a Diffusive Reference Standard for Optical Tissue Phantoms. *Phys. Med. Biol.* **2011**, *56* (2), N21-28.
(39) Chapmann, G.; Paulsen, S.; Zhang, Y. Characterizing long lived intralipid-infused tissue phantoms scattering using imaging sensors. *Proc. SPIE*, **2020**, 11238.
(40) Yang, Y.; Fan, X.; Li, L.; Yang, Y.; Nuernisha, A.; Xue, D.; He, C.; Qian, J.; Hu, Q.; Chen, H.; Liu, J.; Huang, W. Semiconducting Polymer Nanoparticles as Theranostic System for Near-Infrared-II Fluorescence Imaging and Photothermal Therapy under Safe Laser Fluence. *ACS Nano* **2020**, *14* (2), 2509–2521.
(41) Mahesh, M. The Essential Physics of Medical Imaging, Third Edition. *Med. Phys.* **2013**, *40* (7).
(42) Jung, Y.; Jeong, S.; Nayoun, W.; Ahn, B.; Kwag, J.; Kim, G-S.; Kim, S. Quantum dot imaging in the second near-infrared optical window: studies on reflectance fluorescence imaging depths by effective fluence rate and multiple image acquisition. *Journal of Biomedical Optics*. **2015**, 20 (4), 046012.
(43) Jiang, Y.; Huang, J.; Zhen, X.; Zeng, Z.; Li, J.; Xie, C.; Miao, Q.; Chen, J.; Chen, P.; Pu, K. A Generic Approach towards Afterglow Luminescent Nanoparticles for Ultrasensitive in Vivo Imaging. *Nat. Commun.* **2019**, *10* (1), 2064.
(44) Jana, D.; Wang, D.; Rajendran, P.; Bindra, A. K.; Guo, Y.; Liu, J.; Pramanik, M.; Zhao, Y. Hybrid Carbon Dot Assembly as a Reactive Oxygen Species Nanogenerator for Ultrasound-Assisted Tumor Ablation. *JACS Au.* **2021**, *1* (12), 2328–2338.
(45) Srivastava, I., Xue, R., Jones, J., Rhee, H., Flatt, K., Gruev, V., Nie, S. Biomimetic Surface-Enhanced Raman Scattering Nanoparticles with Improved Dispersibility, Signal Brightness, and Tumor Targeting Functions. *ACS Nano* **2022**, 16 (5), 8051-8063.
(46) Srivastava, I., Moitra, P., Fayyaz, M., Pandit, S., Kampert, T. L., Fathi, P., Alanagh, H.R., Dighe, K., Alafeef, M., Vuong, K., Jabeen, M., Nie, S., Irudayaraj, J., Pan, D. Rational Design of Surface-State Controlled Multicolor Cross-Linked Carbon Dots with Distinct

Photoluminescence and Cellular Uptake Properties. *ACS Appl. Mater. Interfaces* **2021**, 13 (50), 59747-59760.
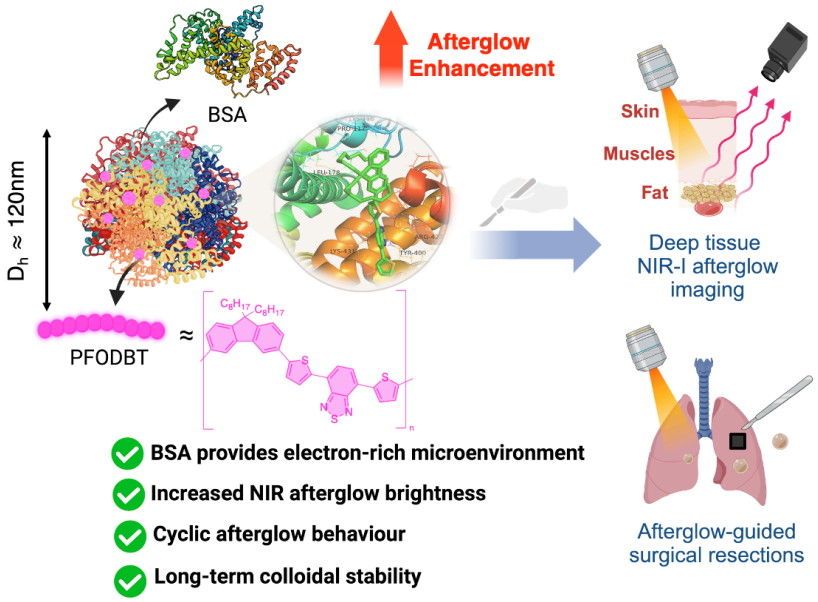
TOC.